Proceedings of ASME Turbo Expo 2025
Turbomachinery Technical Conference and Exposition
GT2025
June 16-20, 2025, Memphis, Tennessee

GT2025-153775

A NEW BODY FORCE-BASED MODELLING APPROACH FOR TURBOMACHINERY AERODYNAMICS: FORMULATION, VERIFICATION AND IMPLEMENTATION ASPECTS

Dimitrios Lamprakis[1,*], Mauro Righi[1], Vassilios Pachidis[1]

[1]Rolls-Royce University Technology Centre, Cranfield University, MK43 0AL, United Kingdom

ABSTRACT

Modelling of turbomachinery flows typically entails single-passage or full annulus RANS and uRANS simulations. The computational and numerical stability challenges associated primarily with transient simulations of multi-stage and coupled turbomachinery components may offset their accuracy benefits. Body force modelling provides a reasonable trade-off between computational efficiency and accuracy, replacing the turbomachinery component with a body force field. In the present work, a new body force-based modelling approach is presented, comprising body force-relevant grids, an inviscid compressible solver in the relative frame of reference with metal and aerodynamic blockage and a new body force model comprising a base turning, correction and viscous force component. Distribution coefficients are introduced, mathematically replicating the spatial distribution of key quantities such as loss and flow deviation using custom functions or CFD data. The proposed approach is sufficiently comprehensive to enable its applicability to all types of compressor and potentially turbine blades, while minimising dependence on CFD input. The validity and limitations of the proposed approach are assessed through numerical response test cases. Subsidiary force components and loss mechanisms, associated with abrupt flow turning and blockage effects are captured. Considerations and modelling aspects regarding grid sensitivity, blockage, the solver and the effect of distribution coefficients on compressor performance are analysed and quantified. Limitations associated with the grid topology, body forces and blockage modelling are partially or fully addressed. The paper aims to provide an in-depth analysis in fundamental aspects of body force modelling approaches, while unveiling obscure aspects and limitations underpinning most body force modelling approaches. A new approach is proposed to mitigate the shortcomings of previous methods.

Keywords: Body force, distribution coefficient, subsidiary forces, through-flow, blockage, turbomachinery, RANS, CFD

*Corresponding author: Dimitrios.Lamprakis@cranfield.ac.uk

NOMENCLATURE

b	blockage parameter
C	distribution coefficient
e	internal energy
E_r	specific relative internal energy
$\boldsymbol{F} = (F_x, F_\theta, F_r)$	body force vector
F_{cor}	correction force
F_{turn}	turning force
F^p_{turn}	subsidiary force component parallel to relative flow path
F_{visc}	viscous force
h	grid spacing
$h_{0,rel}$	total enthalpy in the relative FoR
I	rothalpy
K_{cor}	correction force scaling coefficient
l	coordinate parallel to relative path
L	camberline length
m	meridional coordinate
m_{cor}	corrected mass flow
$\dot{m}$	mass flow
n	spanwise coordinate
P	static pressure
$p_{n\theta,s}$	projection of unit vector $\hat{s}$ on the $n-\theta$ plane
r	radial coordinate
s	coordinate parallel to blade surface and perpendicular to κ / blade pitch length / entropy
t	time
T	static temperature
x	axial coordinate
$\boldsymbol{w} = (w_x, w_\theta, w_r)$	relative velocity vector in cylindrical coordinates
V_{mer}	meridional velocity magnitude
V	magnitude of absolute velocity vector
W	magnitude of relative velocity vector
γ	specific heat ratio
η_{is}	isentropic efficiency
θ	circumferential location
κ	blade metal angle / coordinate parallel to blade profile

Copyright © 2025 by Rolls-Royce plc;
reuse license CC-BY 4.0

λ lean angle
Λ arbitrary scalar property
ν coordinate parallel to turning force on the $m-\theta$ plane
ρ density
σ slip factor
ϕ flow path angle
Ω angular velocity

Abbreviations

CFD computational fluid dynamics
cs camber surface
FoR frame of reference
LE leading edge
MB main blade
ps pressure surface
PR_{tt} total-to-total pressure ratio
$RANS$ Reynolds-averaged Navier-Stokes
SB splitter blade
ss suction surface
TR_{tt} total-to-total temperature ratio
TE trailing edge
VDB vaned diffuser blade

Subscripts

abs property in the absolute FoR
act actual/measured property
CFD property extracted from CFD simulations
cor property related to correction force
imp imposed property
rel property in the relative FoR
$span$ spanwise property
$stream$ streamwise property
sub subdomain property
$visc$ property related to viscous force

Superscripts

$*$ related to numerical flow slippage / modified quantity
$\bar{}$ averaged property

1. INTRODUCTION

Transient, full annulus simulations are required for resolving the flow field in a turbomachinery component primarily when unsteady phenomena extending beyond a blade pitch are expected [1, 2]. These typically entail uRANS simulations which have only recently become feasible due to the excessive associated computational cost. For reference, a computational time of 1-2 months on a 128-core cluster is reported by Fidalgo et al [3] to simulate 20-30 rotor revolutions of the NASA's stage 67 with inlet distortion. Zhao e al [4] report a computational time of one day for a single shaft revolution on 192 cores for full annulus, multi-stage, axial compressor rotating stall and surge uRANS simulations ($\sim 300 \times 10^6$ elements). While GPUs have accelerated some CFD applications, their adoption remains limited due to solver compatibility, required code modifications, and resource constraints in HPC facilities, where CPUs remain predominant [5]. An additional constraint associated with the simulation of the aforementioned unsteady, asymmetric turbomachinery flows are numerical stability challenges. These are linked to local grid resolution, the adequacy of the initial solution, the time-step size, the boundary conditions and the numerical schemes, as reported by Yao et al [6]).

An alternative, computationally efficient modelling approach for turbomachinery components, are body force methods, whereby the bladed component is replaced by a body force-field. Marble [7] was the first to introduce the body force concept, introducing flow turning and losses via source terms. Gong [8] demonstrated the feasibility of simulating inlet distortions, stall inception due to short-wavelength perturbations and rotating stall in axial compressors using a custom 3D Euler solver and body forces. Hsiao et al. [9] used Gong's body force model to simulate NASA's 22" rig at Glenn Research Center [10] (fan stage with nacelle), predicting spanwise pressure and temperature profiles and accurately capturing the flow separation at the intake. Using a 3D Euler solver and body forces, Chima et al. [11] reproduced stall phenomena and assessed the implications of inlet flow distortions on the stability limits of axial compressors. Escuret and Garniet [12] predicted the onset of surge of an axial compressor. Stewart [13] performed axisymmetric, full engine simulations RANS simulations using iterative-based body forces. Longley [14] simulated the transient, post-stall performance of low-speed, axial compressors using body forces. More recently, Righi et al.[2, 15, 16] developed a 3D code with body forces, for axial compressor surge and rotating stall modelling which they validated against multi-stage low-speed and modern high-speed compressors.

Body force models may be classed depending on their approach in four categories [17], following a progression from the most physics-based to the most data-driven models. The first comprises analytical, physics-based models, independent of CFD input. The most important one is Gong's model [8], consisting of a viscous, a blade loading and a flow tangency force component, with the latter two components constituting the turning force. The viscous force is analogous to aerofoil drag and the drag coefficient is estimated by correlations or experimental data. The blades are considered staggered flat plates without curvature. Longley's model [14] follows an identical approach, but includes a streamline curvature term, while the loss model is expressed as a function of total pressure loss. Losses and deviation correlations are used at forward flow conditions and purely axial flow is assumed. Righi et al. [15] combined Brand's [18] and Longley's model, while cascade performance quantities such as deviation and pressure losses are estimated by empirical correlations. None of the above models accounts for blade leaning. Additionally, the flow tangency component is scaled with a tuning coefficient, a simplified representation of the spatial blade geometry is assumed and the flow is considered axial, thus their applicability is restricted to axial flow compressors only. Peters [19] modified Gong's model to account for blade lean which introduced a radial component. Hall's [20] turning force model consists of a single turning force component without calibration coefficients but assumes incompressible flow. The second class of models comprises analytical models coupled with CFD-derived quantities. Brand [18] derived an improved version of Gong's model, accounting for curvature effects omitting blade lean and flowpath curvature, limitations which were later addressed by Kottapalli's model [21], extending its applicability to centrifu-

Copyright © 2025 by Rolls-Royce plc;
reuse license CC-BY 4.0

gal compressors. Both models are dependent on extensive CFD input for the estimation of the deviation gradient parameter and the entropy gradient. The viscous force models are similar to Gong's. No flow tangency component is included. Prescribed outflow conditions are not imposed, thereby losses and deviation are allowed to vary according to the state of the flow. The third category comprises methods whereby the geometry is immersed into the grid cells. The most representative model of the third category is the immersed boundary method with smeared geometry (IBMSG) approach of Cao et al [22]. The flow turning source terms are computed explicitly at each passage cell by solving the momentum equations in the direction normal to the local blade wall "hidden" inside the mesh cells. The last category includes methods whereby the body force-field is extracted directly from RANS simulations. A database is generated, providing estimations of the body forces as a function of flow-field variables. This approach was implemented for the simulation of an axial compressor by Kiwada [23] and a centrifugal compressor by Benneke [24] stage.

Another essential aspect, primarily related to the mass flow capacity of the turbomachinery component are blockage effects. This is particularly true for wedge-type vaned diffuser passages which introduce substantial metal blockage, while an aerodynamic blockage of the order of 17% can be found in impellers, even at forward flow conditions as reported by Eisenlohr et al. [25]. Modifications in the governing equations to account for metal but not transient aerodynamic blockage effects are reported in the literature [17, 21–24] but these are restricted to absolute FoR formulations, which from a numerical stability point of view, are less adequate when a large fraction of the computational domain rotates, e.g. impellers [26]. Errors regarding the evaluation of blockage gradient terms using finite difference approximations are also reported by Kiwada [23], primarily in the vicinity of the LE and TE.

The first objective of the present paper is to propose a universally applicable, physics-based, through-flow modelling approach for turbomachinery applications, by addressing constraints of existing approaches. These primarily include decoupling the body force model from extensive CFD input, ensuring its applicability irrespective of the turbomachinery component geometry, improving its accuracy with computationally efficient methods, modelling metal and aerodynamic blockage effects as well as exploring adequate grid strategies and solvers. The second objective is to assess the validity and limitations of the proposed approach following a systematic verification with numerical response test cases. The final objective is to unveil, quantify and address the implications of modelling aspects underpinning relevant body force applications, such as subsidiary losses due blockage effects and flow turning, momentum imbalance due to misestimation of blockage gradient terms, unnatural flow behaviour due to excessively high correction force interference and directional grid sensitivity.

2. COMPUTATIONAL DOMAIN AND SOLVER

2.1 Grid generation

The computational domain is structured within the geometric boundaries defined by the hub and shroud aero lines of the compressor duct. The topology of the computational domain is structured following three principal considerations; numerical stability, formation of continuous body force-fields and generation of computationally efficient, structured grids. Herein, the flow is modelled as inviscid, thus mesh refinements near shroud and hub endwalls to capture the boundary layer are unnecessary. The grid topology is defined by synthesising subdomains representative of ducted or bladed domains, thus their boundaries are aligned with the LE and TE of each blade, forming distinct ducted or bladed domains. These types of grids will be referred to hereafter as *geometry-adaptive*. Bladed regions are more susceptible to numerical instabilities due to large flow-field gradients and high turning forces, thus a denser streamwise grid resolution is essential. The node distribution in both directions primarily utilises an equidistant distribution algorithm. In-between domains with different streamwise cell size however, the algorithm switches to an exponential distribution to gradually match the cell size of the adjacent domain. This is strictly applied to non-bladed domains.

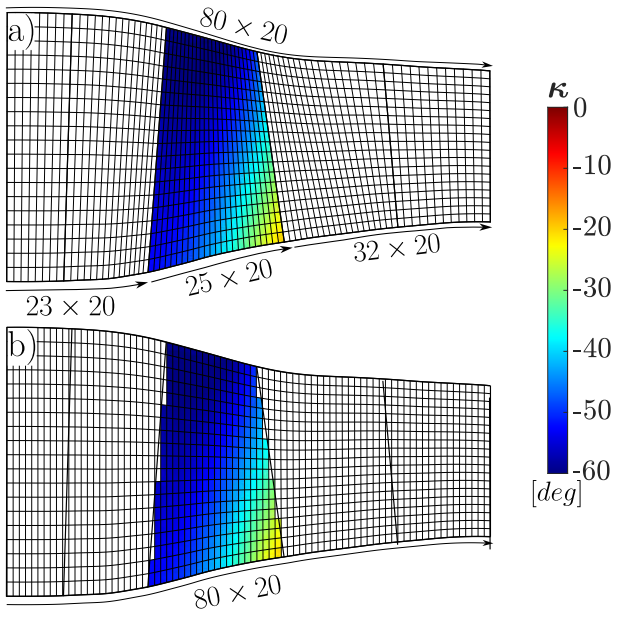


FIGURE 1: BLADE ANGLE DISTRIBUTION AND COMPUTATIONAL DOMAIN OF ROTOR 37 [27] FOLLOWING A) GEOMETRY-ADAPTIVE AND B) UNIFORM APPROACH.

A comparison of two rotor 37 [27] grids generated following the two approaches along with the blade angle distribution contours are shown in Fig.1. The blade angle contours indicate the cells positioned within the bladed domain and by extension, in the body force domain. Both grids are built in both directions with an identical number of elements. It is evident that the uniform approach contains a superfluous number of elements in the inlet and outlet ducted regions. The bladed region, which is critical from a numerical stability and energy exchange point of view, is discretised with a relatively coarse grid, while the misalignment of the gridlines and the blade's LE and TE at the boundaries of the bladed domain, results in a locally discontinuous body force field. This entails numerical stability and increased computational cost implications. A substantial increase in the number of elements in the streamwise direction would be required 1) to ensure suffi-

Copyright © 2025 by Rolls-Royce plc;
reuse license CC-BY 4.0

cient grid resolution inside bladed domains to prevent potential numerical stability issues and 2) to provide a reasonably accurate body force field near the LE and TE. Spanwise discretisation is less critical for numerical stability, since the blade angle gradients are larger in the streamwise direction; this is exacerbated near the LE particularly when the flow is approaching at a high incidence. However, it defines to a great extent, the accuracy of the generated body force representation of the blade. This is essential as the blade curvature at the LE and TE dictates the overall flow turning and ultimately, the energy exchange with the flow. If blockage is included in the analysis, additional errors will be introduced. The aforementioned deficiencies are reasonably addressed by the geometry-adaptive grid generation approach. A minimum of approximately 40×10 elements is typically required to achieve acceptable flow control and numerical stability in both axial compressor blades and impellers.

2.2 Solver

The flow-field solution is obtained transiently by solving the conservation form of the unsteady, compressible, Euler equations in the relative FoR by time-marching until a steady state is reached. The flow herein is considered axisymmetric ($\partial/\partial\theta = 0$), however the proposed modelling approach can easily be extended to non-axisymmetric flows. A blockage parameter, b, is introduced in the governing equations, reducing the effective cell face areas and volumes due to both metal and aerodynamic blockage. The blockage parameter is iteratively updated according only to the state of the flow (pseudo-transient) and represents the ratio of the effective over the entire area/volume, thus $b \in [0, 1]$. To adequately resolve compressible, transonic flows of high-speed aero-engine compressors, the developed solver utilises Godunov's numerical scheme coupled with the HLLC approximate Riemann solver, reformulated in the relative FoR to obtain the convective fluxes [28]. The HLLC scheme was chosen due to its computational efficiency and accuracy [28], as well as its proven effectiveness in a similar through-flow code for rotating stall and surge in axial compressors developed by Righi et al. [15]. Forward time-stepping discretisation is used for computational efficiency, thus the derived solution is first-order accurate in space and time. This is expected to introduce substantial numerical diffusion compared to higher-order schemes for the fluxes e.g. MUSCL and the time-marching e.g. Runge-Kutta methods [28]. Viscous dissipation and flow turning are introduced via body force source terms. The governing equations in conservation form are given below:

$$\frac{\partial b\rho}{\partial t} + \nabla \cdot (b\rho \boldsymbol{w}) = 0 \tag{1}$$

$$\frac{\partial (b\rho w_x)}{\partial t} + \nabla \cdot (w_x (b\rho \boldsymbol{w})) = -\frac{\partial (bP)}{\partial x} + P\frac{\partial b}{\partial x} + b\rho F_x \tag{2}$$

$$\frac{\partial (b\rho w_\theta)}{\partial t} + \nabla \cdot (b\rho w_\theta \boldsymbol{w}) = -\frac{\partial (bP)}{\partial \theta} + P\frac{\partial b}{\partial \theta} - 2b\rho\Omega w_r + b\rho F_\theta \tag{3}$$

$$\frac{\partial (b\rho w_r)}{\partial t} + \nabla \cdot (w_r b\rho \boldsymbol{w}) = -\frac{\partial (brP)}{\partial r} + P\frac{\partial b}{\partial r} + b\frac{P}{r} + 2b\Omega w_\theta \rho + \rho b\Omega^2 r + b\rho F_r \tag{4}$$

$$\frac{\partial (b\rho E_r)}{\partial t} + \nabla \cdot (b\rho \boldsymbol{w}\, I) = 0 \tag{5}$$

2.3 Blade curvature definition

The blade curvature in space is defined by three angles, shown in Fig. 2; blade metal angle, flow path angle and lean angle. The derivative of the first expresses the curvature of the blade's camberline and is the angle between the meridional vector, $\hat{\boldsymbol{m}}$ and the camberline vector, $\hat{\boldsymbol{\kappa}}$. The derivative of the second designates the local duct curvature along the meridional plane and is the angle between $\hat{\boldsymbol{m}}$ vector and the axial vector, $\hat{\boldsymbol{x}}$. The third describes the lean of the blade in the circumferential direction. It is the angle between the vector normal to the meridional one, $\hat{\boldsymbol{n}}$ and the blade's mean lines, expressed by vector $\hat{\boldsymbol{s}}$, on the $(n-\theta)$ plane. The spatial angle distribution is computed using a vector analysis approach on a discretised camber surface domain. The camber surface grid is generated using 3D pressure and suction side coordinates of each blade via piecewise interpolating polynomials (cubic splines). This ensures that the polynomials pass though the given points, while providing higher-order approximations in-between the given coordinates. Pressure and suction surface domains are subsequently generated to extract the local blade metal blockage distribution.

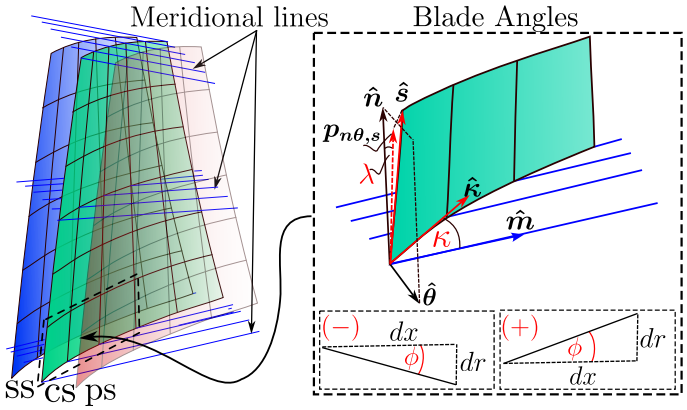


FIGURE 2: BLADE SURFACE GRIDS AND DEFINITION OF BLADE ANGLES AND VECTORS FOR THE EVALUATION OF THE BLADE CURVATURE.

3. BODY FORCE MODEL

3.1 Turning force model

The *turning force* acts perpendicular to the actual relative path, thus flow turning is by definition isentropic. It is a function of the local flow-field and the local curvature of the imposed relative path. The curvature of the ideally intended relative path coincides with that of the local camberline of the blade, expressed by the local blade metal angle, κ. To account for flow deviation, an *effective* camberline may be defined, the curvature of which, is expressed by the locally imposed relative flow angle, $\beta_{imp} = \kappa + \delta$. Since the deviation angle is not a priori known, it may be extracted from experimental data, CFD simulations (see [18, 21, 24]) or from component-specific empirical loss correlations. In the second approach, local deviation angles along the blade domain can be extracted and the imposed relative flow path can be explicitly defined at all cells inside blade domains. In the latter approach, a mathematical function is required in order to distribute the predicted deviation angle in bladed domains.

Copyright © 2025 by Rolls-Royce plc;
reuse license CC-BY 4.0

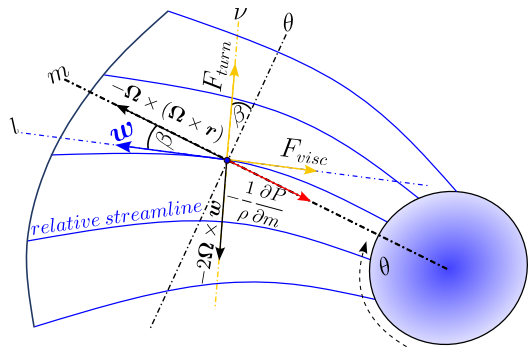


FIGURE 3: FORCE BALANCE ALONG A RELATIVE STREAMLINE INSIDE A ROTOR.

The basis of the turning force model is derived by considering the momentum balance along a relative streamline (see Fig. 3) using the Lagrangian form of the Euler equations in the relative frame of reference (FoR) and assuming steady-state conditions. The body force-field is considered axisymmetric, acting as if an infinite number of blades was guiding the flow ($\partial/\partial\vartheta = 0$). The momentum is consequently expressed according to Eq. (6).

$$(\boldsymbol{w}\cdot\nabla_m)\,\boldsymbol{w} = -\frac{1}{\rho}\nabla_m P - 2\boldsymbol{\Omega}\times\boldsymbol{w} - \boldsymbol{\Omega}\times(\boldsymbol{\Omega}\times\boldsymbol{r}) \tag{6}$$

The left (LHS) and right hand sides (RHS) of Eq. (6) can be expanded in natural coordinates as follows:

$$LHS = w\left(\frac{\partial w}{\partial l}\hat{\boldsymbol{l}} + \frac{\partial \hat{\boldsymbol{l}}}{\partial l}w\right) = w\left(\frac{\partial w}{\partial l}\hat{\boldsymbol{l}} - \frac{\partial \beta}{\partial l}\hat{\boldsymbol{v}}\right) \tag{7}$$

$$RHS = -\frac{1}{\rho}\frac{\partial P}{\partial m} + \frac{sin\phi}{r}[w_\theta + \Omega r]^2 \tag{8}$$

The component normal to the relative path is $-w\frac{\partial\beta}{\partial l}$ and expresses the relative streamline curvature term. Projecting the RHS of Eq. (8) normal to the flow path direction, and substituting Eqns. (7) and (8) into Eq. (6), the turning force component is derived:

$$F_{turn} = -\frac{1}{\rho}\frac{\partial P}{\partial \nu} - w^2\left(\frac{\partial\beta}{\partial l} + \frac{sin\beta sin\phi}{r}\right) + 2\Omega w sin\phi + \Omega^2 r sin\beta sin\phi \tag{9}$$

The pressure gradient term in Eq. (9) is associated with instabilities [18, 21] but its destabilising effect can be dissipated by introducing a correction force similar to that of Gong [8]. Its presence might be particularly unstable if strong local pressure gradients are present, e.g. compressor stall, therefore it is replaced by performing an influence coefficient analysis [29] analogous to Brand [18] and Kottapalli [21] (see Appendix). The base turning force component is finally given by Eq. (10):

$$\begin{aligned} F_{turn} = w^2 &\left[\frac{cos\beta\left((2\gamma-1)\,Ma_{rel}^2 - tan^2\beta + 1\right)}{(2\gamma-1)\,Ma_{rel}^2+1}\frac{\partial\beta}{\partial m}\right. \\ &\left. + \frac{\frac{Ma_\Omega^2}{Ma_{rel}^2} + (2\gamma-1)\,Ma_{rel}^2 + 2}{(2\gamma-1)\,Ma_{rel}^2+1}\frac{sin\phi sin\beta}{r}\right] + 2w\Omega\,[sin\phi] \\ &+ \Omega^2 r\,[sin\phi sin\beta] + F_{visc}\left[-\frac{tan\beta\left(\frac{1}{Ma_{rel}^2} + (\gamma-1)\right)}{(\gamma-1)\,R}\right] \end{aligned} \tag{10}$$

Contrary to Kottapalli's and Brand's formulations, the formulation does not exhibit singularity since the denominator never approaches zero as Ma_{mer} approaches unity, thus not requiring additional treatment near sonic conditions. However, the turning force approaches infinity as the imposed blade angle approaches 90^o, thus the imposed flow angle is limited to 88°, preventing excessively high turning forces to be imposed. Additionally, the blade outflow condition is explicitly defined, i.e. a prescribed amount of pressure loss and flow turning is imposed.

3.2 Correction force model

The turning force model constitutes the main/base component force, however inside a time-dependent flow-field, local flow variables may be subject to substantial gradients. These may induce local misalignment of the flow, severely compromising the ability of the turning force model to accurately impose the prescribed outflow angle condition. This was observed even without the presence of strong gradients with most turning force models in the literature.

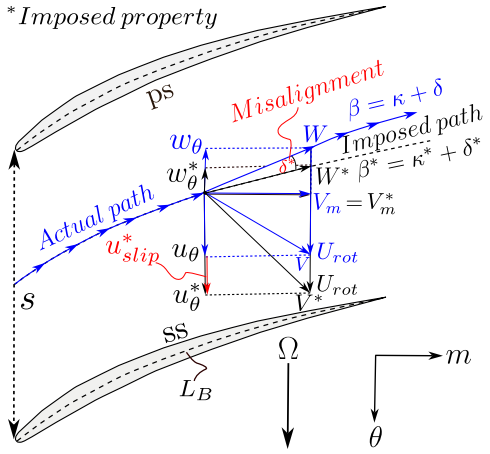


FIGURE 4: OVERVIEW OF CORRECTION FORCE MODEL VELOCITY COMPONENTS DUE TO FLOW MISALIGNMENT WITH RESPECT TO THE IMPOSED RELATIVE PATH.

This is addressed by introducing an additional force component, which will be referred to herein as *correction force*. The coupling of a main turning force with an additional correction

Copyright © 2025 by Rolls-Royce plc;
reuse license CC-BY 4.0

force component is reported in other studies focusing on rotating stall and surge simulations in axial compressors [8, 14, 15]. None of these models was found sufficiently effective for impeller and vaned diffuser blades applications. The formulation of the present model is based on the concept of numerical slip. The magnitude of the applied correction force is transiently adjusted via a numerical slip factor coefficient in the absolute FoR, as per Eq. (11). The numerical slip essentially expresses the circumferential momentum flux deficit or surplus required to introduce the prescribed flow turning at a given mass flow. This is reflected on the velocity triangles shown in Fig. 4 depicting the velocity components of the misaligned flow and the ones corresponding to a perfectly guided flow, denoted with *. Assuming constant meridional velocity, i.e. independent of slip, to ensure mass flow conservation, the circumferential velocity components in Eq. (11) can be expressed as follows:

$$\sigma_{cor} = \frac{u_{\theta,act}}{u_{\theta,imp}} = \frac{u_{\theta,act} + \Omega r}{u_{\theta,imp} + \Omega r} = \frac{V_{mer} tan\beta_{act} + \Omega r}{V_{mer} tan\beta_{imp} + \Omega r} \tag{11}$$

The corresponding numerical slip velocity, $u_{slip,cor}$ due to the misestimation of turning force can be expressed as:

$$u_{slip,cor} = u_{\theta,act} - u_{\theta,imp} = u_{\theta,act}\left[\frac{\sigma_{cor} - 1}{\sigma_{cor}}\right] \tag{12}$$

The correction force is expressed as a function of the correction slip velocity, $u_{slip,cor}$, the meridional velocity, V_{mer} and a scaling coefficient, K_{cor}, which in conjunction with the slip velocity, adjusts the magnitude of the correction force. The local camberline or geometric meridional streamline lengths are the most appropriate characteristic lengths as they are independent of the local radial position, introducing a gradual augmentation of correction force interference towards the shroud due to the reduction of the blade length. The K_{cor} coefficient essentially constitutes a tuning parameter and is typically set to a fixed value in the range $K_{cor} = [0.8 - 2] \cdot 10^2$ for axial compressor blades and $K_{cor} = [5 - 20] \cdot 10^2$ for impeller and vaned diffuser blades. These ranges were determined from multiple through-flow simulations carried out in several axial and centrifugal compressor geometries. Excessively high values may trigger numerical instabilities and unrealistic flow behaviour. The correction force is exerted parallel to the turning force and in its expanded form is given by Eq. (13):

$$F_{cor} = K_{cor}\frac{|V_{mer}|\left(w_{\theta,act} + \Omega r\right)}{L_c}\left[1 - \frac{V_{mer} tan\beta_{imp} + \Omega r}{w_{\theta,act} + \Omega r}\right] \tag{13}$$

3.3 Viscous force model

The *viscous force* is acting parallel to the relative flow path, thereby constituting a source term with strictly positive entropy generation. The generated entropy manifests as a reduction in the relative stagnation pressure relative to the ideal one, as shown in Fig.5.

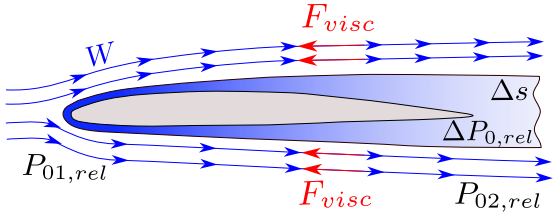


FIGURE 5: VISCOUS FORCE ACTING PARALLEL AND OPPOSITE ALONG A RELATIVE STREAMLINE GENERATING ENTROPY AND PRESSURE LOSS.

The viscous force model is derived analytically by combining Marble's viscous force expression, Gibbs equation, the differential form of rothalpy and the flow path angle (Eqns. (9) - (17)):

$$\boldsymbol{F_{visc}} = \frac{\partial s}{\partial l} T\hat{\boldsymbol{l}} = \frac{\partial s}{\partial m} T cos\beta\hat{\boldsymbol{l}} \tag{14}$$

$$T_{0,rel} ds = dh_{0,rel} - \frac{1}{\rho} dP_{0,rel} \tag{15}$$

$$dI = dh_{0,rel} - \frac{1}{2} d\left(\Omega^2 r^2\right) \tag{16}$$

$$\sin\phi = \frac{dr}{dm} \tag{17}$$

Combining the above equations, the viscous force model is expressed by Eq. (18). This formulation addresses the need for extensive CFD simulations to obtain the entropy gradient (see [18, 21]) by replacing it with stagnation pressure loss, which can be obtained using for example component-specific, empirical loss correlations.

$$F_{visc} = cos\beta\frac{P}{\rho}\left\{\frac{1}{P_{0,rel}}\frac{\partial P_{0,rel}}{\partial m} - \left(\frac{\gamma \sin\phi}{1 + \frac{\gamma-1}{2} Ma_{rel}^2}\right)\frac{Ma_\Omega^2}{r}\right\} \tag{18}$$

The second term in the brackets represents the relative stagnation enthalpy which in an adiabatic flow with no energy addition is identical to the isentropic one. Any imbalance, by means of relative stagnation pressure loss, will generate entropy. The presence of the flow path angle ϕ and Ma_Ω, accounts for variations in streamline curvature and the additional kinetic energy it entails in a rotating domain. By extension, its contribution is significant in rotating impellers and negligible in stators and fully axial flows. The average pressure loss along the rotor domain is distributed by introducing the corresponding viscous force distribution coefficient, modified since the imposed pressure loss is not the average but rather the aggregate one. The viscous force can then be approximated by Eq. (19).

$$F_{visc} = cos\beta\frac{P}{\rho}\left\{\frac{1}{P_{0,rel}}\frac{\Delta P_{0i,rel} - C^*_{visc}(m,n)\overline{\Delta P}_{0,rel}}{\Delta m} - \left(\frac{\gamma \sin\phi}{1 + \frac{\gamma-1}{2} Ma_{rel}^2}\right)\frac{Ma_\Omega^2}{r}\right\} \tag{19}$$

Copyright © 2025 by Rolls-Royce plc;
reuse license CC-BY 4.0

3.4 Distribution coefficients

The *distribution coefficient* mathematically describes the local distribution of any flow-field variable inside the body force-field domain. An average cascade quantity, herein, total pressure loss and flow deviation, can be distributed by coupling it with a distribution coefficient. This facilitates the evaluation and implementation of the turning and viscous force components, while providing a method for distributing these terms.

Extracting coefficients directly from CFD simulations, e.g. steady state RANS simulations, enables complex, viscous-induced phenomena such as endwall boundary layer growth, tip leakage vortices, etc., to be captured and subsequently reconstructed in the through flow domain. Custom coefficients, e.g. uniform, sinusoidal, etc., are incapable of reproducing such flow features, but constitute a simplified, CFD-independent modelling approach. Regardless of the approach, the average state of the distributed property in the body force domain should be identical, thereby not affecting global aerodynamic performance predictions. That might not always be the case, if for instance unrestrained flow separation or flow reversal is induced by the coefficient, compromising the ability of the body force model to impose the prescribed amount of deviation or loss.

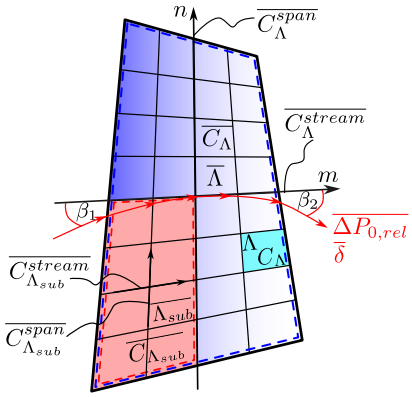


FIGURE 6: SUBDOMAINS USED FOR THE EXTRACTION OF DISTRIBUTION COEFFICIENTS.

The distribution coefficient is defined as the ratio of the local to the average value of a variable along a direction, plane or volume. The average of a consistently defined coefficient should be equal to unity, $\overline{C_\Lambda} = 1$. Three approaches to derive these coefficients are proposed: (i) average, (ii) piecewise, and (iii) cell-based/interpolated approach (see Fig. 6). The first, approximates the distribution by combining averaged distributions of the entire passage. The second, follows a similar approach but the passage is divided into subdomains, while the latter is derived directly using information at a cell scale. Given a pitchwise averaged flow-field, extracted from single passage RANS simulations, distribution coefficients in the streamwise and spanwise direction are according to Eqs. (20)-(21).

$$C_\Lambda^{stream}(m) = \frac{\Lambda(m)}{\overline{\Lambda}_{stream}} = \frac{\Lambda(m)}{1/\Delta m \int_{m_1}^{m_2} \Lambda(m)dm} \tag{20}$$

$$C_\Lambda^{span}(n) = \frac{\Lambda(n)}{\overline{\Lambda}_{span}} = \frac{\Lambda(n)}{1/\Delta n \int_{n_1}^{n_2} \Lambda(n)dn} \tag{21}$$

Equations (20)-(21) entail the intrinsic assumption that C_Λ^{stream} and C_Λ^{span} are independent of n and m coordinate respectively. In practice, the coefficients can vary substantially from hub to tip or from LE to TE, but averaging them typically provides a representative distribution of the entire domain. A single 2D integration could be an alternative approach, but was avoided as in strongly non-uniform flows it could disproportionately be influenced by local flow phenomena such as local flow separations, compromising its accuracy. The 1D averaging method better preserves dominant flow trends, avoids biases from uneven grid distributions, and remains computationally efficient. Spatial averaging is preferred to avoid biasing the extracted distribution based on flow properties, e.g. mass flow which are not necessarily conserved along each geometric stream and span position. This could further exacerbate the smoothening out effect induced by the averaging process of local flow features. The averaged coefficients may be combined into a single, total distribution coefficient $\overline{C_\Lambda}(m,n)$ providing the full distribution of any variable Λ along the $(m-n)$ plane using Eq. (22). This is schematically illustrated in Fig. 6, where the blue region represents the entire blade domain, defined by merging two averaged coefficients in the streamwise and spanwise directions.

$$\overline{C_\Lambda}(m,n) = \overline{C_\Lambda^{span}}(n)\,\overline{C_\Lambda^{stream}}(m) \tag{22}$$

To better capture shorter lengthscale features, which would be lost due to the averaging process over the entire blade domain, the averaging region may be partitioned in subdomais within which, local averaged coefficients are defined. In Fig. 6, the blade domain (blue) is discretised in four subdomains (red) inside which coefficients are locally evaluated and denoted by the subscript (sub). By adjusting the integration limits and introducing a scaling coefficient, $C_{\Lambda_{sub}}^{cor}$, in each subdomain to scale the local average quantity, $\overline{\Lambda_{sub}}$, the coefficient can be defined in a piecewise manner, in accordance to Eq. (23). Scaling is necessary as the average state of the distributed property within each subdomain varies, and is by extension inconsistent with the one of the overall blade domain. This would result in a mismatch between the prescribed and actual average property inside the domain and $\overline{C_\Lambda} \neq 1$.

$$\overline{C_{\Lambda_{sub}}}(m,n) = C_{\Lambda_{sub}}^{cor}\,\overline{C_{\Lambda_{sub}}}(m,n) \tag{23}$$

where $C_{\Lambda_{sub}}^{cor}$ the scaling coefficient given by Eq. (24).

$$C_{\Lambda_{sub}}^{cor} = \frac{\overline{\Lambda_{sub}}}{\overline{\Lambda}} \tag{24}$$

If the flow-field variable inside the body force field domain are known at each grid point, no averaging process is necessary. The spatial distribution of the coefficient can then be directly interpolated from the computational grid.

$$C_\Lambda(m,n) = \frac{\Lambda(m,n)}{\overline{\Lambda}} \tag{25}$$

Copyright © 2025 by Rolls-Royce plc;
reuse license CC-BY 4.0

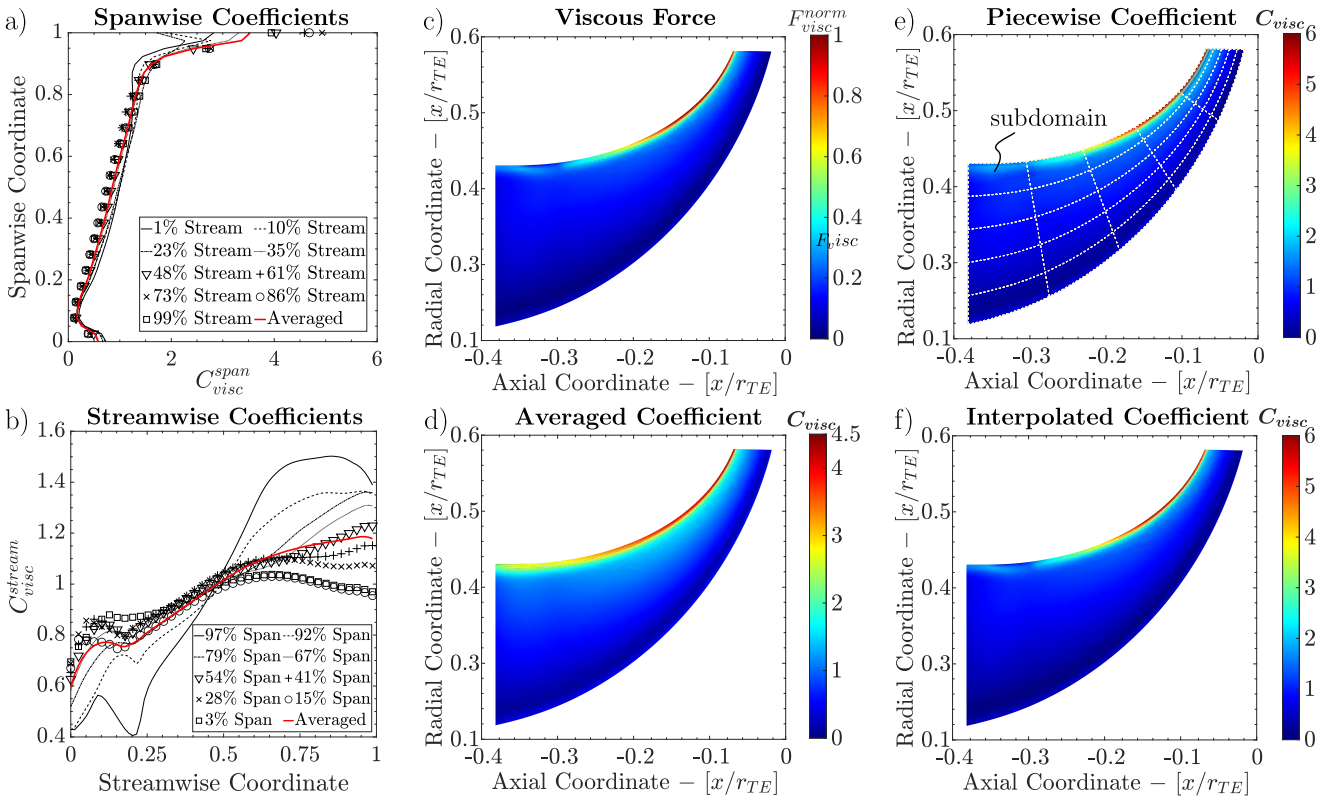


FIGURE 7: A) SPANWISE AND B) STREAMWISE DISTRIBUTION COEFFICIENTS AT DIFFERENT STREAMWISE AND SPANWISE LOCATIONS RESPECTIVELY, C) CFD-EXTRACTED VISCOUS FORCE DISTRIBUTION AND VISCOUS FORCE COEFFICIENTS DERIVED FOLLOWING THE D) AVERAGE, E) PIECEWISE AND F) INTERPOLATED CELL-BASED APPROACH.

Figure 7c visualises the pitchwise averaged, normalised viscous force distribution in the impeller SRV2 passage [25]. The extraction of the viscous force, was carried out at the LE and TE to avoid negative local meridional entropy gradient values as discussed in [18, 21]. Despite the limitations of the approach, the high entropy region near the shroud due to flow separation is captured. The spanwise and streamwise coefficients are plotted at different locations, from LE to TE and from hub to tip respectively in Fig. 7a,c along with the averaged distributions, shown in red. The averaged coefficient derived by the coalescence of the averaged directional coefficients according to Eq. (23) is plotted in Fig. 7d. Despite the averaging, the coefficient reproduces the high entropy region near the shroud reasonably well, although this region is extended further upstream towards the LE. The piecewise coefficient, shown in Fig. 7e is derived on a 5×5 subdomain matrix, reconstructing the viscous force field with remarkable accuracy and alleviating the errors of the previous one. The discrepancies are more notable in the subdomain located in the vicinity of the TE and the shroud. The interpolated coefficient (Fig. 7f) is the most accurate one since it does not entail averaging and entirely relies on interpolated values from the original dataset. The averaged coefficient is the most efficient approach, in terms of database size, but can be particularly inaccurate if the quantity drastically varies locally. For CFD-derived coefficients, the interpolation method is the recommended approach, since the piecewise one is rather complicated. The averaged approach despite its limitations can be combined with custom coefficients; in practice the streamwise distribution is rather trivial for the state of the flow-field downstream of the blade in an axisymmetric flow-field. It is the C^{span} which ultimately will dictate the accuracy of the flow-field downstream of the blade passage, thus a simple uniform C^{stream} coupled with a CFD-derived C^{span} downstream the TE, is sufficient to reconstruct a realistic, physics-informed flow-field.

4. THROUGH-FLOW GRID SENSITIVITY

To determine appropriate grid requirements, in terms of mesh resolution for body force-based through-flow methods, geometry-adaptive grids of the rotor 37 and impeller SRV2 are assessed with different levels of refinement in the spanwise and streamwise direction. The first series of grids increases the number of streamwise elements uniformly across all domains while keeping the spanwise resolution constant. The second series refines the spanwise resolution without altering the streamwise grid density. Richardson extrapolation is performed using data from 4 grids with a constant refinement ratio of 2 to approximate quantities of infinite grid resolution, $\Lambda_{(h=0)}$ (not all grids are shown on the graphs). The imposed pressure loss, deviation and boundary conditions are identical for all operating points. No blockage effects are considered in the analysis. All quantities are normalised with their corresponding extrapolated values. Figure 8a shows the directional grid sensitivity analysis of rotor 37, with the axis on top designating the number of streamwise elements in the bladed domain. For the streamwise analysis, 20 elements are used in the

Copyright © 2025 by Rolls-Royce plc;
reuse license CC-BY 4.0

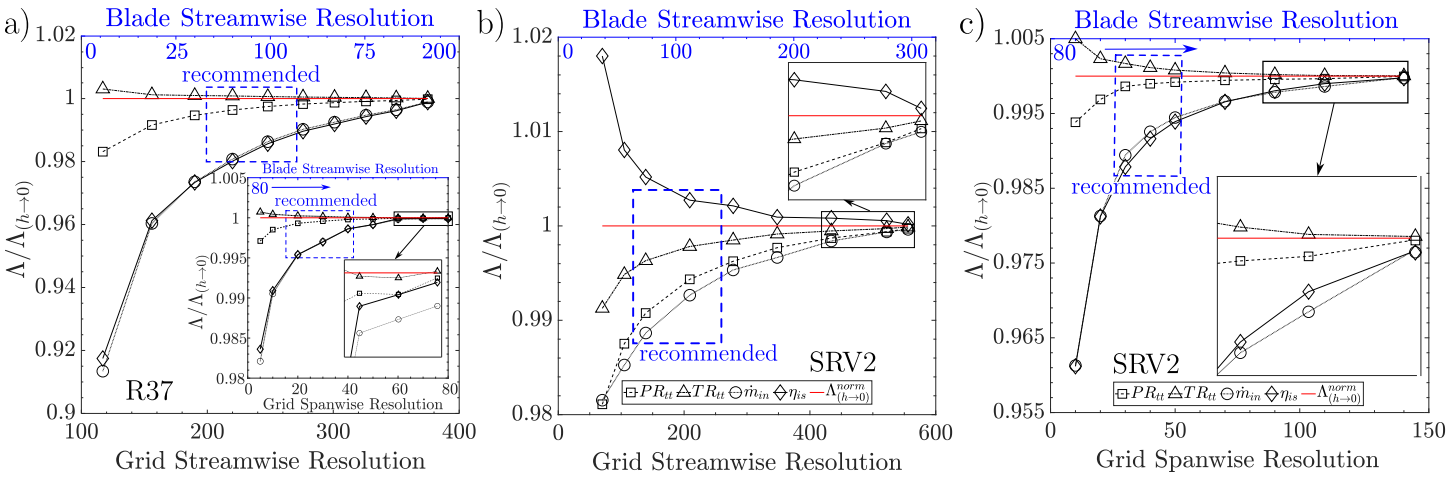


FIGURE 8: STREAMWISE AND SPANWISE GRID SENSITIVITY ANALYSIS: ROTOR 37 (A) AND IMPELLER SRV2 (B, C).

spanwise direction. The pressure and temperature ratio discrepancies between the exact (red line) and the lowest resolution grid are less than 1.7% and 0.3% respectively, but the efficiency and mass flow are underestimated by 8.3% and 8.7% respectively. These errors are primarily related to the inaccurate body force representation of the blade and the inability of the body force model to precisely impose the prescribed flow turning. A reasonable balance between numerical efficiency and accuracy is achieved when the bladed domain is discretised with [80 – 100] elements, decreasing the errors to less than 2.5% and 2% respectively. For the spanwise grid sensitivity (bottom right of Fig. 8a), the number of streamwise elements in the bladed domain was held constant to 80. Evidently, the spanwise resolution of the grid in axial blades is not expected to introduce any noteworthy errors, allowing for coarse spanwise discretisation; increasing the spanwise resolution to 10 and 20 cells reduces the errors to less than 1% and 0.5% for all quantities respectively.

A similar sensitivity analysis is carried out on the impeller SRV2 geometry, shown in Fig. 8b,c. For the streamwise analysis, a constant number of 30 spanwise elements is selected. The normalised compressor quantity curves indicate that contrary to rotor 37, the streamwise dependency of impeller SRV2 is rather insignificant. This is evident by the errors which do not exceed 2% in the coarsest grid comprising 40 elements in the bladed domain. Doubling the refinement, limits the maximum errors to less than 1%, thus a resolution in the range [60 - 80] cells in the bladed domain provides sufficient accuracy and stability. However, the impeller displays a substantially higher sensitivity in the spanwise grid resolution compared to axial blades (Fig. 8). The coarsest grid, discretised with 10 cells in the spanwise direction, introduces mass flow and efficiency errors of 3.9%. Increasing the spanwise resolution to 30 and 40 elements reduces the maximum errors to less than 1.3% and 0.8% respectively. Therefore, the suggested spanwise resolution is within the range [20 – 40].

The grid analysis indicates a higher sensitivity of the principal compressor performance quantities with the physically smaller dimension of the simulated blade (streamwise for axial blades and spanwise for impellers). In impellers, the larger physical domain of the blade facilitates control of the flow, requiring less streamwise elements compared to axial compressor blades, reducing flow turning errors. These errors are deemed adequate for preliminary design/performance assessment as they are comparable with the ones of typical, medium-sized grids used for conventional 3D RANS turbomachinery simulations.

5. SUBSIDIARY FORCE MECHANISMS

To fully understand the potential implications of the turning force and the blockage modelling approach, it is important to identify and attempt to quantify them. The turning force is ideally exerted perpendicular to the local relative streamline. This is not entirely feasible due to flow misalignment and numerical errors. This inevitably generates a component parallel to the flow which typically generates a *subsidiary parallel force* component, F_p^{turn}.

To assess its impact, "isentropic" characteristics of rotor 37, i.e. without explicitly imposing a viscous force component, are obtained at 60% speed, as shown in Fig. 9a. The presence of loss mechanisms throughout the entire characteristic of rotor 37 is evident by the efficiency characteristic, shown in Fig. 9a. At the two highest mass flow operating points, a blade passage shock wave forms, imparting additional losses which cannot be dissected from the subsidiary ones. Beyond that point, the flow remains subsonic, thereby enabling the association of the measured losses entirely with F_p^{turn}, which in this case acts as a viscous force. The interference of the subsidiary, parallel force component progressively increases as mass flow decreases, due to the higher incidence angle.

The spatial distribution of F_p^{turn} can be visualised using Eq. (18), with a positive sign indicating a force against the direction of motion (viscous force), as shown in Fig 9b. A high viscous force region in the vicinity of the LE is captured. These manifest due to the abrupt flow turning once the flow enters the bladed domain, attempting to change the direction of the incoming flow to match the blade angle at the LE. Except for the increased misalignment, the magnitude of the parallel component is further amplified due to the very high turning forces required to impose the prescribed flow turning. Plotting the spanwise isentropic efficiency distribution (Fig. 9c), unveils the presence of higher

Copyright © 2025 by Rolls-Royce plc;
reuse license CC-BY 4.0

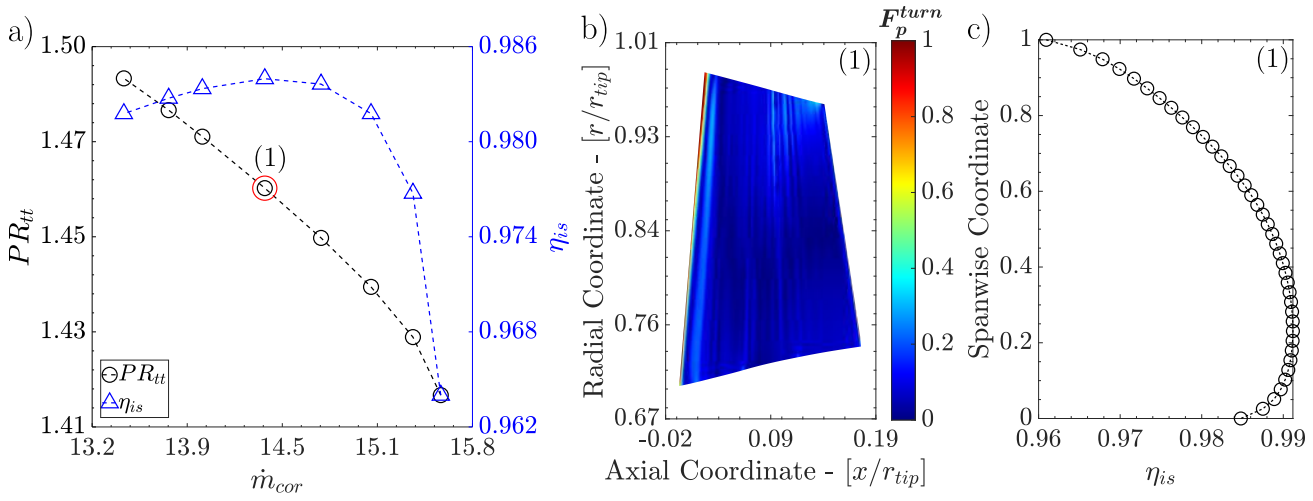


FIGURE 9: A) 'ISENTROPIC' PRESSURE AND EFFICIENCY CHARACTERISTICS OF ROTOR 37 AT 60% SPEED, B) DISTRIBUTION OF SUBSIDIARY PARALLEL FORCE AND C) SPANWISE ISENTROPIC EFFICIENCY DISTRIBUTION DOWNSTREAM THE TE.

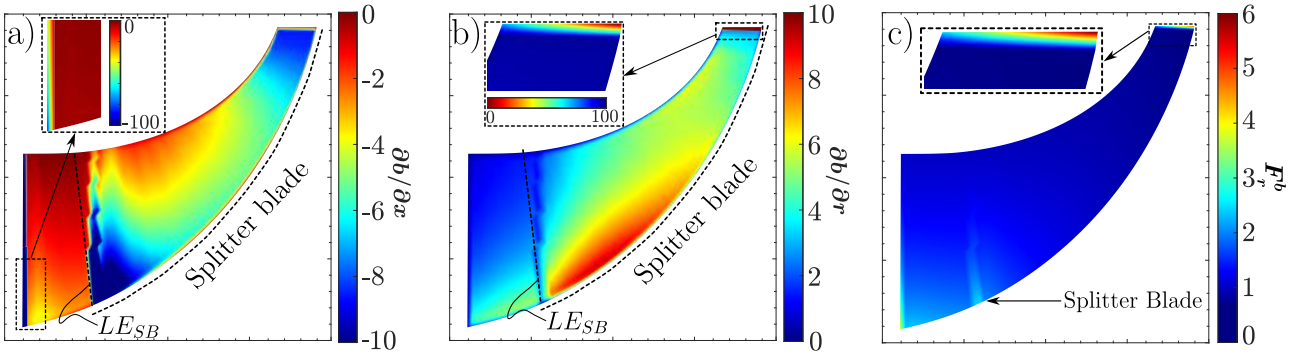


FIGURE 10: SRV2 IMPELLER A) AXIAL AND B) RADIAL BLOCKAGE GRADIENT TERM DISTRIBUTIONS, C) RADIAL COMPONENT OF SUBSIDIARY FORCE RELATED TO BLOCKAGE GRADIENT TERMS.

entropy regions extending from midspan to shroud as well as close to the hub. These are in agreement with the subsidiary parallel force contour and the turning force distribution (not shown here). Towards the shroud, blade angles increase, requiring higher flow turning forces, thereby amplifying the contribution of the parallel component.

Another subsidiary force generation mechanism originates from inaccuracies related to the evaluation of the blockage gradient terms, $\partial b/\partial r$ and $\partial b/\partial x$. These terms designate the pressure forces acting on the blocked fraction of the cells and any misestimation will result in momentum imbalance. The blockage gradient terms are initially evaluated using central finite differencing and subsequently re-evaluated with the proposed approach; they are directly retrieved from the momentum equations, using the trivial solution of a stagnant, zero-pressure gradient flow-field. These terms are only function of the spatial blockage distribution and not the flow-field (of course their presence will affect it), thus they could be derived from any known flow-field. This provides an exact, local evaluation of the terms, entirely eliminating errors. The gradient terms, computed with the proposed approach, are depicted in Fig. 10a,b, with the zoomed regions highlighting the areas where the terms have their highest magnitude. The distribution of subsidiary forces in the radial direction, F_r^b, originating from errors in the evaluation of the $\partial b/\partial r$ (finite difference) is retrieved from the radial momentum imbalance and is depicted (normalised) in Fig. 10c. The largest subsidiary force components are exerted in the vicinity of the main and splitter blade LE and TE, where blockage changes abruptly due to the transition from/to ducted domains and presence of additional blades. For reference, these force generate streams of forward and reverse flow of velocity up to 20% the speed of sound.

Blockage modelling errors are not exclusively associated with the blockage gradient terms; the blockage essentially modifies the volume and face areas of the cells, introducing mesh-related errors. This is of particular importance when the blockage between 2 adjacent cells changes abruptly (radial domains with thick blades), potentially introducing numerical errors, e.g. vaned, wedge-type diffusers. The meridional blockage distribution of NASA CC3 compressor with wedge type vaned diffuser [30] is shown in Fig. 11a. Modified, smoothened distributions of different levels are investigated, aiming to mitigate blockage-related numerical implications. These are $3rd$ order polynomials passing through prescribed (m,b) points (adjustable) with continuous/matching gradients at the blending point. For the highest smoothening setting, the offset between the blending point and the LE/TE is about 30% of the blade's meridional length.

Copyright © 2025 by Rolls-Royce plc;
reuse license CC-BY 4.0

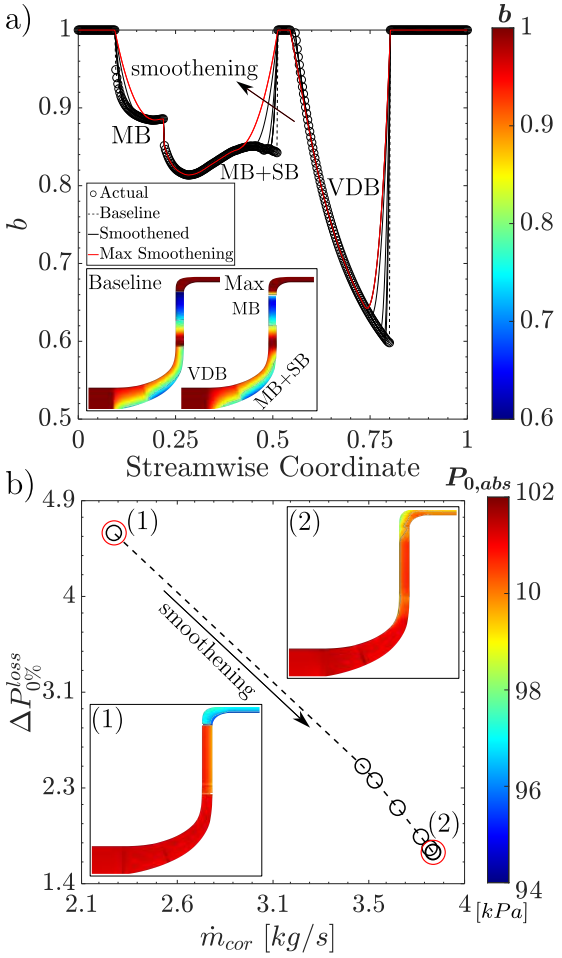


FIGURE 11: A) ACTUAL AND MODIFIED BLOCKAGE DISTRIBUTIONS OF NASA CC3 COMPRESSOR AND B) TOTAL PRESSURE LOSS FOR DIFFERENT LEVELS OF BLOCKAGE SMOOTHENING.

Modelling the NASA CC3 duct without body forces and only including blockage effects, a significant pressure loss of approximately 4.8% is measured for the baseline model (Fig. 11b). The location of the pressure loss is just downstream the vaned diffuser TE, where the flow exits the bladed domain. Applying smoothening functions mitigates this phenomenon, reducing the loss to less than 1.6%. In that case the loss is not associated with blockage but rather with a flow separation downstream the vaned diffuser TE, near the shroud. An alternative approach would be the readjustment of the grid to be proportional to the actual, effective size of the cells, but that could be rather restrictive if substantial unsteady aerodynamic blockage effects are modelled. For thick, wedge-type vaned diffusers, setting the blending point 10-15% upstream of the TE is sufficient to reduce losses to less than 2%, which is considered a reasonable trade-off between accuracy for preliminary design calculations and minimising the extent of geometry alteration. Smoothening will inevitably alter the local flow-field, resulting in a progressively higher diffusion in the modified portion of the blade, without however modifying the total amount of diffusion that would otherwise occur. Consequently, in an inviscid through-flow method, the outflow conditions are not expected to be substantially affected, which is important if loss/deviation predictions are dependent on inflow/outflow conditions e.g. empirical correlations. It should also be noted, that smoothening is typically only applied to thick vaned diffuser blades and not all blades.

6. CURVATURE ERRORS

As discussed earlier, the LE and TE flow angles largely define the energy exchange with the flow, while the curvature at the throat affects the local pressure/velocity field and turbulence. This in turn affects the choking mass flow of the component. Figure 12 shows a comparison of the computed and experimentally measured impeller SRV2 blade angle distribution at the hub and the shroud. At the shroud, the errors at the aforementioned, critical locations are less than 2%, while the corresponding errors at the hub do not exceed 4%. Errors within the same range were recorded with the proposed curvature evaluation approach in other axial compressors blades and impellers, thus the expected error band lies within [1% - 4%]. The errors are primarily associated with the interpolation scheme used to generate the camber surface grid as well as the resolution of the grid. These are deemed adequate for preliminary design, particularly for centrifugal compressors where energy is primarily imparted due to change in the streamline radius and secondarily due to flow turning effects.

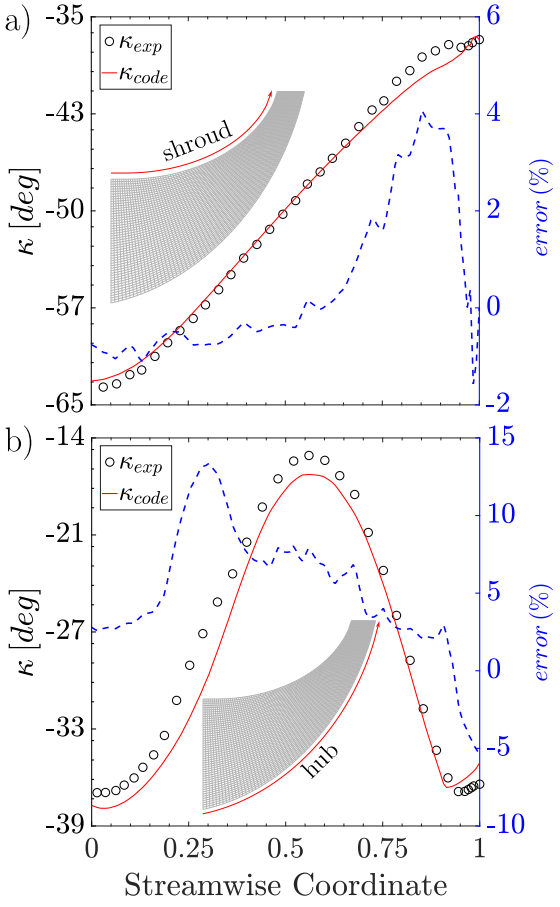


FIGURE 12: COMPARISON OF EXPERIMENTAL AND ESTIMATED BLADE ANGLE DISTRIBUTIONS AT (A) SHROUD AND (B) HUB OF IMPELLER SRV2.

Copyright © 2025 by Rolls-Royce plc;
reuse license CC-BY 4.0

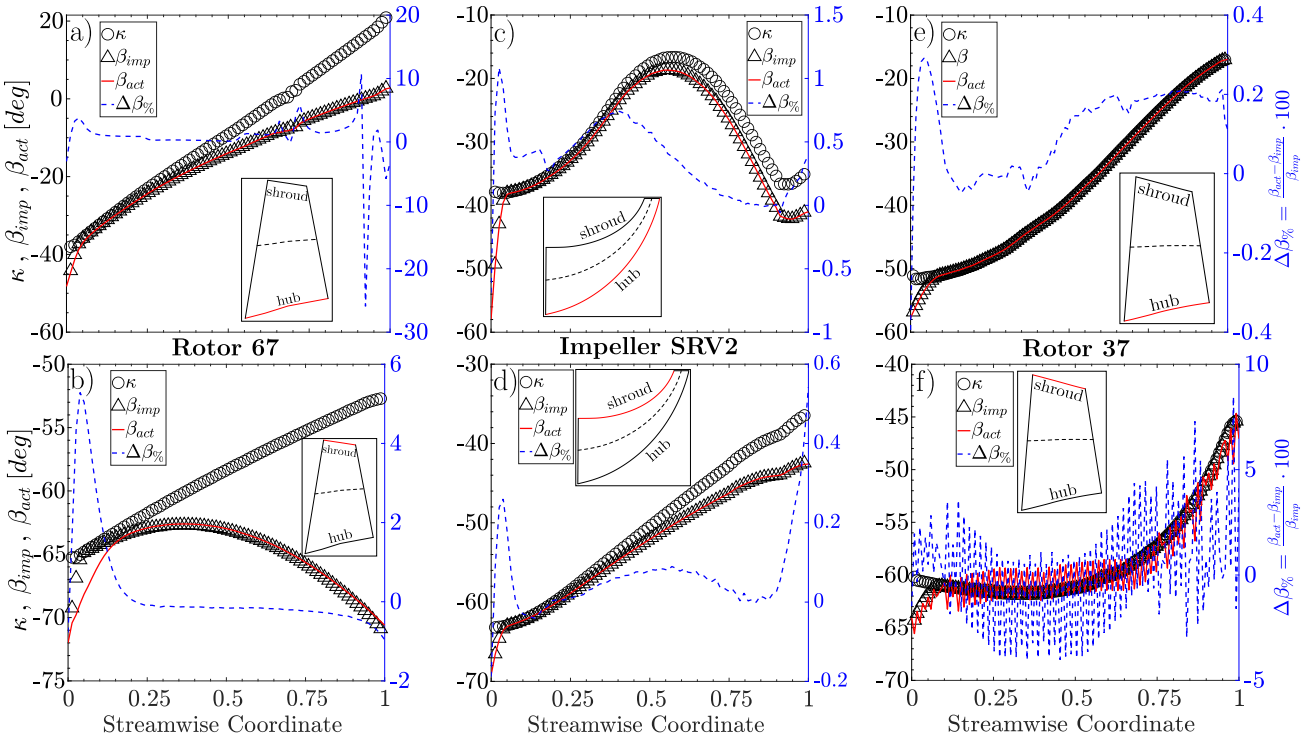


FIGURE 13: MERIDIONAL DISTRIBUTION OF BLADE ANGLE (CIRCLES), IMPOSED FLOW ANGLE (TRIANGLES) AND ACTUAL FLOW ANGLE AT HUB AND SHROUD OF ROTOR 67, IMPELLER SRV2 AND ROTOR 37.

7. BODY FORCE MODEL - VALIDITY AND LIMITATIONS

7.1 Turning force model

The capabilities and limitations of the present turning force model, formed by merging the contribution of both the base turning and the correction force, is assessed using three rotor geometries: NASA rotor 67 [31], impeller SRV2 and rotor 37. The streamwise blade metal, κ, imposed (β_{imp}) and actual β_{act} relative flow angle distributions of all rotor blades are plotted at the hub (top) and the shroud (bottom), along with the corresponding misalignment errors, $\Delta\beta_{\%}$.

The blade and flow angle distributions of rotor 67 are plotted in Fig. 13a,b. A deviation angle is imposed and is uniformly distributed in all directions. The correction coefficient is set to $K_{cor} = 1.2 \cdot 10^2$. At both the hub and the shroud, the flow is well aligned with the imposed relative flow path. As previously discussed, the energy input is entirely dependent on the flow angles of the incoming and outcoming flow, thus misalignments inside the blade passage are trivial from an energy exchange point of view. Significant misalignment however in the vicinity of the throat may introduce errors in the predicted choking mass flow. The errors at the hub and the shroud near the throat are less than 0.9% and 1.7% respectively, while the corresponding errors at the TE do not exceed 3.3% and 0.96% respectively. These are deemed sufficiently accurate for preliminary design purposes. The higher errors near the shroud's LE are due to abrupt turning of the flow, which is carefully controlled to ensure numerical stability.

Figures 13c,d, show the angle distributions at the hub and the shroud of impeller SRV2. The correction coefficient is set to $K_{cor} = 16 \cdot 10^2$, to compensate for the larger camberline length. In this case, K_{cor} is sufficiently high to precisely guide the flow even in the vicinity of the LE, where an abrupt flow turning is imposed. The misalignment errors along the entire span do not exceed 1%. For the last test case, rotor 37 is selected, the angle distributions of which, are shown in Fig. 13e,f. The correction force coefficient is set to $K_{cor} = 2 \cdot 10^2$ substantially increasing the interference of the correction force, becoming the dominant component. At the hub, the imposed and actual relative paths are in excellent agreement as indicated by the misalignment errors which do not exceed 0.3%. Near the shroud, the higher flow turning, increased relative velocities and reduced camberline length - translating to higher F_{cor}, precipitate excessive turning forces, primarily driven by the correction force. The excessive interference of the correction force results in local overshoots and undershoots as shown in Fig. 13f. This typically manifests in the higher mass flow regimes, i.e. near choking, thus K_{cor} should be adjusted adjusted at high flow conditions so that flow control is preserved near the throat and the TE, without K_{cor} exceeding the critical value (in this case about $K_{cor} \approx 1.9 \cdot 10^2$) . Alternatively, K_{cor} could be locally defined but this would introduce an additional level of complexity and calibration.

7.2 Viscous force model

The amount of viscous dissipation introduced in the flow, expressed in terms of total relative stagnation pressure gradient, is not a priori known, thus its accuracy is dependent upon the prediction approach e.g. CFD, loss correlations, etc. Regardless of the approach, it is essential to assess the ability of the model to introduce the prescribed pressure loss. Three test cases are selected: rotor 37 rotating at 60% speed, impeller SRV2 stationary

Copyright © 2025 by Rolls-Royce plc;
reuse license CC-BY 4.0

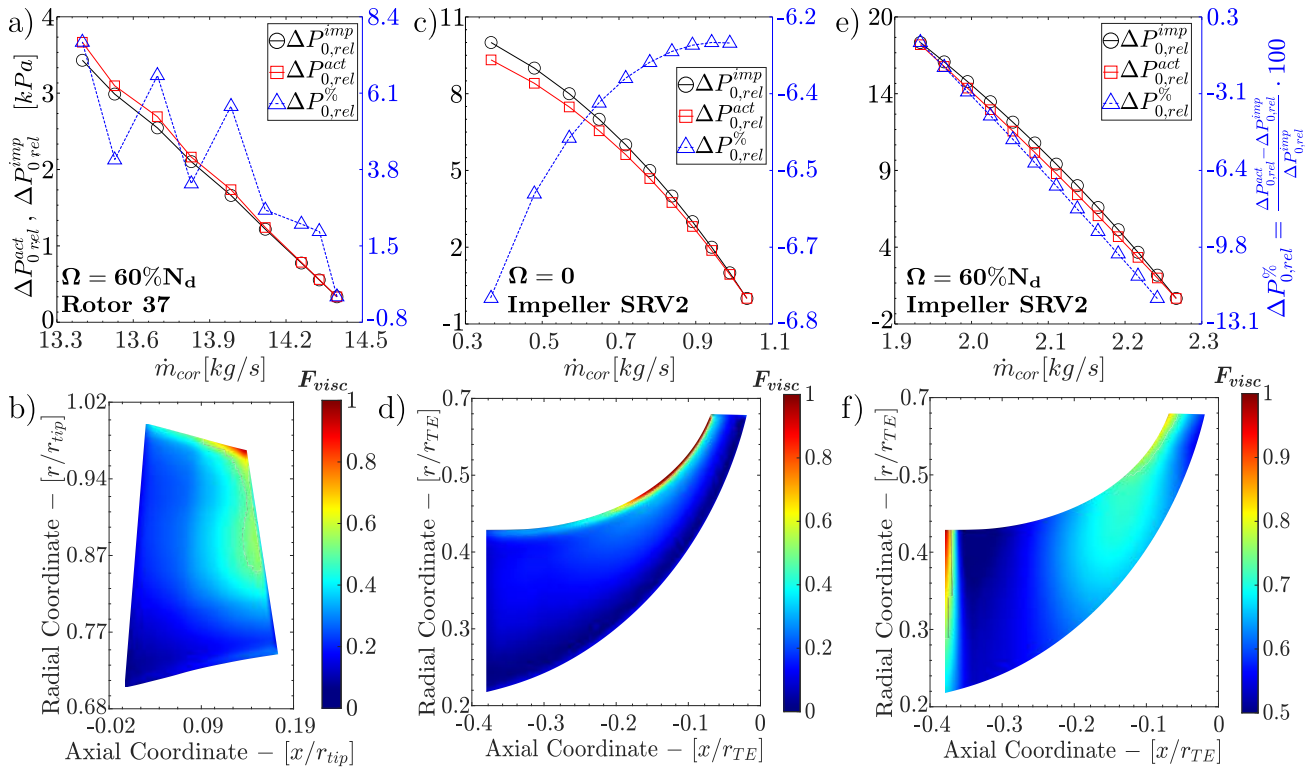


FIGURE 14: COMPARISON OF IMPOSED VS. ACTUAL TOTAL PRESSURE LOSS AND VISCOUS FORCE DISTRIBUTION IN BLADE PASSAGES OF ROTOR 37 (LEFT) AND IMPELLER SRV2 WITH UNIFORM (MIDDLE) AND CFD-EXTRACTED DISTRIBUTION COEFFICIENT (RIGHT).

and rotating at 60% speed. These aim to assess the validity of the model in axial compressor rotors, stators and impellers. Different operating points are obtained by applying constant boundary conditions and varying the amount of imposed pressure loss in the blade passage. The boundary conditions are selected and adjusted to prevent additional entropy generation due to formation of shock waves. To limit the implications of subsidiary losses in the measured pressure loss, the first operating point corresponds to an isentropic rotor; the pressure loss introduced by the isentropic rotor is then removed from all subsequent measurements.

Figures 14a,b depict the imposed and actual total pressure loss in the relative FoR, the corresponding errors and the distribution of the imposed viscous force inside rotor 37 blade passage. For the latter, a CFD-extracted distribution coefficient is used. The pressure loss is gradually increased from [0 - 3.5kPa] and is compared against the average pressure loss downstream the TE. The measured losses are in very good agreement with the imposed ones, in the mid to low loss region, not exceeding 3.4%. The errors exhibit an increasing trend as the prescribed pressure loss increases, reaching 7.63% at the highest pressure loss setting. This discrepancy is presumably related to variations in subsidiary losses, as the mass flow and incidence angle change and cannot be entirely eliminated by a single reference point. A similar comparison is carried out in impeller SRV2, shown in Fig. 14c. A CFD-extracted distribution coefficient (Fig. 14d) is applied and the blade is modelled as a stator ($\Omega = 0$). The measured losses are in very good agreement but consistently lower than the imposed ones, while the errors gradually increase at the higher pressure loss region, from 6.3% to 6.8%. This indicates an almost constant offset (percentage wise) which could be attributed to subsidiary losses. To further verify the validity of the viscous force model, the rotational speed is set to 60%, i.e. $N_d = 30000rpm$. Pressure losses are distributed uniformly and the prescribed losses are scaled by a correction factor, proposed by Aungier [32], to account for changes in the mean streamline radius. In the mid to high pressure loss region (Fig. 14e), the errors range between [0.84% - 6.1%] and keep increasing continuously, reaching approximately 12% in the lowest loss setting. In the lower loss range, the small magnitude of the imposed losses exacerbates the errors, which in practice represent trivial discrepancies, corresponding to less than than 0.2kPa and 0.33kPa for the lowest loss settings respectively. Despite the usage of a uniform loss distribution coefficient, increased viscous forces at the LE can be seen in Fig. 14, indicative of the presence of subsidiary force components, while downstream variations are mainly related to changes in the flow angle, pressure and density (see Eq. (18). The response test cases indicate that the proposed viscous-distribution modelling approach is capable of introducing the prescribed loss with reasonable accuracy at a range of different operating conditions regardless of the blade geometry. Despite the effort to eliminate sources of subsidiary loss mechanisms, quantifying the errors associated with the present model entails a degree of uncertainty as their implications depend on the state of the flow and cannot entirely be segregated. The errors are considered satisfactory for preliminary design calculations and are expected to be less significant compared to errors introduced by the loss and deviation/slip prediction methods (for example empirical correlations models).

Copyright © 2025 by Rolls-Royce plc;
reuse license CC-BY 4.0

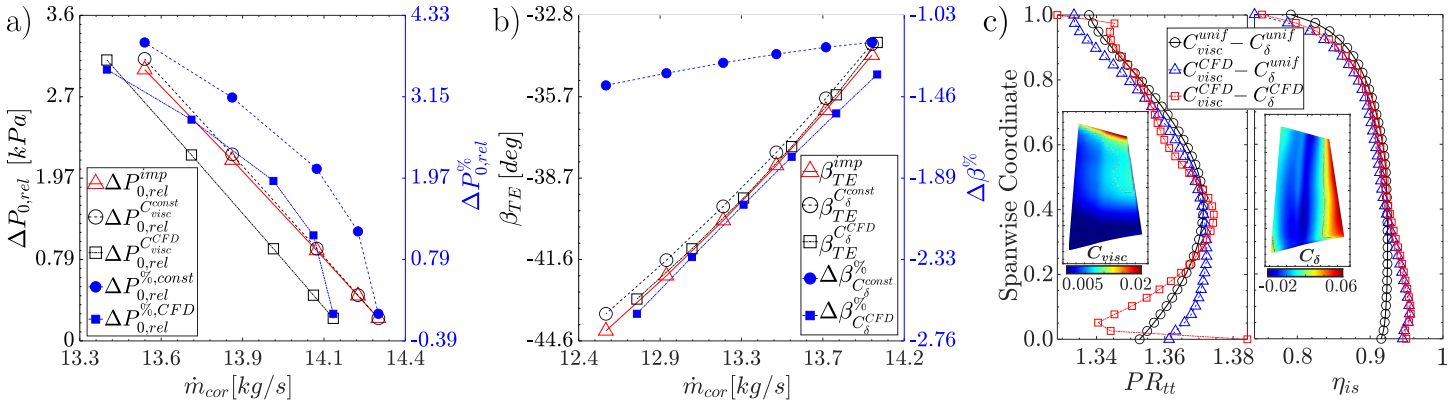


FIGURE 15: COMPARISON OF IMPOSED AND ACTUAL A) LOSSES AND B) FLOW ANGLES DOWNSTREAM OF R37 TE USING UNIFORM AND CFD-DERIVED DISTRIBUTION COEFFICIENTS. SPANWISE PROFILE OF PR_{tt} AND η_{is} OBTAINED WITH DIFFERENT COEFFICIENTS (C).

8. DISTRIBUTION COEFFICIENTS AND AERODYNAMIC PERFORMANCE

As discussed earlier, distribution coefficients should preserve the average state of the flow. This hypothesis is assessed via 2 test cases using rotor 37 geometry; for the first, a range of pressure losses without flow deviation is imposed, while the latter entails the imposition of different deviation angles in an isentropic flow. An identical pressure gradient is maintained across all simulations. Metal blockage effects are included in both cases and results are obtained using uniform and CFD-derived distribution coefficients. The latter are shown in Fig. 15c. The imposed pressure loss (red triangles), averaged losses derived by uniform coefficient (empty circles) and CFD coefficient through-flow simulations (empty rectangles), as well as the corresponding errors (filled markers) are shown in Fig. 15a. The measured losses, obtained with both coefficients, are in very good agreement with the imposed ones, with a maximum error of 3.94% recorded at the highest pressure loss setting with a uniform coefficient. The recorded errors gradually increase, as higher losses are imposed with the uniform coefficient model, exhibiting consistently slightly higher discrepancies. A notable difference between the two datasets is the massflow offset; even though the boundary conditions and the imposed losses are identical, the operating points differ but are moving along the same characteristic. The imposed and measured flow angles are shown in Fig. 15b. The measured flow angles correlate well along the entire sweep. The errors are below 2.61% throughout the entire sweep, while the uniform coefficient model is consistently more accurate. The previously observed offset in mass flow is drastically reduced. The negative errors indicate that less than the prescribed deviation is applied. The results further confirm the validity of the body force model and the distribution coefficient concept both from a mathematical and an implementation point of view.

The effect of the different coefficients on the spanwise distribution of the aforementioned quantities is illustrated in Fig. 15c. Compared to the uniform coefficient (black circles), the CFD viscous coefficient increases the losses near the shroud (blue triangles), replicating the high entropy generation region due to the mixing-out of the tip leakage vortex, while diminishing the imposed losses at lower span positions. This is reflected on the reduced pressure rise and efficiency, compared to the uniform distribution, near the shroud endwall. Replacing the uniform deviation coefficient with a CFD-derived one has a negligible effect on the efficiency distribution. This is expected as it constitutes an inherently flow-turning aspect and is therefore isentropic, however it significantly alters the local work input and by extension, the PR_{tt} distribution. This is particularly evident near the shroud and the hub where the actual deviation distribution differs substantially from the uniform one. The errors fall well within an acceptable range for preliminary design, with loss discrepancies translating to less than 0.5% efficiency drop, while flow turning errors have negligible impact on pressure rise and efficiency. Additionally, these errors are secondary to uncertainties in standard empirical models.

9. SUMMARY AND CONCLUSIONS

A comprehensive body force-based approach for turbomachinery aerodynamics is developed. The proposed through-flow framework entails a solver in the relative FoR with metal and aerodynamic blockage, a new physics-based body force model derived from first principles coupled with distribution coefficients, as well as grid and blade curvature definition methods. The validity of the proposed through-flow framework is assessed by carrying out numerical response test cases, while unveiling obscure, yet practical aspects in the process. Methods to address these aspects and limitations of previous methods are proposed, covering fundamental and implementation considerations. The main conclusions are summarised below:

1. A grid topology aligned with the meridional projection of the blades is essential for the formation of uniform body force-fields in the vicinity of the LE and the TE. Axial compressor blades are substantially more sensitive to the streamwise resolution of the grid, while impellers are more sensitive to the spanwise resolution. Grid size boundaries are proposed, providing a reasonable trade-off between computational efficiency and accuracy, reducing errors to less than 2%.

2. The vector-based, blade curvature evaluation method is validated against impeller SRV2, with errors of 1–4% primarily linked to interpolation.

Copyright © 2025 by Rolls-Royce plc;
reuse license CC-BY 4.0

3. The existence and origins of subsidiary forces and loss mechanisms is for the first time identified. These are related to abrupt flow turning at the LE and momentum imbalance due to misestimation of the blockage gradient terms. An efficiency drop of up to 1.81% is recorded due to abrupt flow turning in rotor 37. Additional losses due to inadequate blockage modelling at the duct/bladed component interfaces are reported, resulting in up to 4.8% pressure loss. A smoothening method is proposed to mitigated it.

4. A new turning force model is derived, incorporating a base turning force and a correction force without inherently relying on CFD input and is verified against rotor 67, impeller SRV2 and rotor 37. Near the TE, flow misalignment does not exceed 3.3% and 1% for the first and second geometry respectively, while the errors near the throat do not exceed 1.7% in both cases. Significant interference of the correction force however may result in unnatural flow behaviour, primarily near the shroud.

5. A new viscous force model, applicable to all types of blades is developed, based on fundamental principles and relating entropy generation with relative stagnation pressure losses. The discrepancies between the prescribed and the measured losses were found mostly in the range [0%-7%], with the reported errors being exacerbated as the interference of subsidiary forces cannot be entirely eliminated.

6. Distribution coefficients are mathematically defined and coupled with critical cascade quantities: deviation and pressure loss. These can be directly extracted from CFD simulations, recasting complex, viscous-induced flow features in body-force simulations. While these coefficients modify the spatial distribution of these quantities, they preserve the average state of the quantity, with the corresponding errors not exceeding 3.94%.

ACKNOWLEDGMENTS

The authors would like to thank Rolls-Royce plc. for supporting and allowing the publication of this work. Special thanks to Richard Tunstall, Steven Mazur and John Harvell for supervising this work.

REFERENCES

[1] Espinal, D., Im, H.-S., and Zha, G.-C., 2017, "Full-annulus simulation of nonsynchronous blade vibration excitation of an axial compressor," *Journal of Turbomachinery,* **140**(3), March, p. 031008.

[2] Righi, M., Pachidis, V., and Könözsy, L., 2020, "On the prediction of the reverse flow and rotating stall characteristics of high-speed axial compressors using a three-dimensional through-flow code," *Aerospace Science and Technology,* **99**(105578).

[3] Fidalgo, V. J., Hall, C. A., and Colin, Y., 2012, "A study of fan-distortion interaction within the nasa rotor 67 transonic stage," *Journal of Turbomachinery,* **134**(5), May 051011.

[4] Zhao, F., Dodds, J., and Vahdati, M., 2018, "Poststall behavior of a multistage high speed compressor at off-design conditions," *Journal of Turbomachinery,* **140**(12), October, p. 121002.

[5] Niemeyer, K. E., and Sung, C.-J., 2014, "Recent progress and challenges in exploiting graphics processors in computational fluid dynamics," *Journal of Supercomputing,* **67**, pp. 528–564.

[6] Yao, J., Gorrell, S. E., and Wadia, A. R., 2010, "High-fidelity numerical analysis of per-rev-type inlet distortion transfer in multistage fans—part i: Simulations with selected blade rows," *Journal of Turbomachinery,* **132**(4), May 041014.

[7] Marble, F. E., 1964, *Aerodynamics of Turbines and Compressors*, Vol. 10 of *High Speed Aerodynamics and Jet Propulsion* Princeton University Press.

[8] Gong, Y., 1999, "A computational model for rotating stall and inlet distortions in multistage compressors," Ph.d. thesis, Massachusetts Institute of Technology.

[9] Hsiao, E., Naimi, M., Lewis, J. P., Dalbey, K., Gong, Y., and Tan, C., 2001, "Actuator duct model of turbomachinery components for powered-nacelle navier-stokes calculations," *Journal of Propulsion and Power,* **17**(4), pp. 919–927.

[10] Jeracki, R. J., Topol, D. A., Ingram, C. L., Larkin, M. J., Roche, C. H., and Thulin, R. D., 2004, Advanced subsonic technology (ast) 22-inch low noise research fan rig preliminary design of adp-type fan 3 Tech. Rep. NASA/CR-2004-212718, NASA Glenn Research Center, February.

[11] Chima, R. V., 2006, "A three-dimensional unsteady cfd model of compressor stability," In Proceedings of Turbo Expo: Power for Land, Sea, and Air, Vol. 6, pp. 1157–1168.

[12] Escuret, J., and Garnier, V., 1994, "Numerical simulations of surge and rotating-stall in multi-stage axial-flow compressors," In 30th Joint Propulsion Conference and Exhibit.

[13] Stewart, M. E. M., 1995, "Axisymmetric aerodynamic numerical analysis of a turbofan engine," In Proceedings of Turbo Expo: Power for Land, Sea, and Air, Vol. 2, p. V002T02A013.

[14] Longley, J. P., 2007, "Calculating stall and surge transients," In Proceedings of Turbo Expo: Power for Land, Sea, and Air, Vol. 6, pp. 125–136.

[15] Righi, M., Pachidis, V., Könözsy, L., and Pawsey, L., 2018, "Three-dimensional through-flow modelling of axial flow compressor rotating stall and surge," *Aerospace Science and Technology,* **78**, pp. 271–279.

[16] Righi, M., Pachidis, V., Könözsy, L., Giersch, T., and Schrape, S., 2022, "Experimental validation of a three-dimensional through-flow model for high-speed compressor surge," *Aerospace Science and Technology,* **128**(107775).

[17] Thollet, W., 2017, "Body force modeling of fan-airframe interactions," PhD thesis, Institut Supérieur de l'Aéronautique et de l'Espace.

[18] Brand, M. L., 2013, "An improved blade passage model for estimating off-design axial compressor performance," M.sc. thesis, Massachusetts Institute of Technology.

[19] Peters, A., 2014, "Ultra-short nacelles for low fan pressure ratio propulsors," Ph.d. thesis, Massachusetts Institute of Technology.

Copyright © 2025 by Rolls-Royce plc;
reuse license CC-BY 4.0

[20] Hall, D. K., 2015, "Analysis of civil aircraft propulsors with boundary layer ingestion," Ph.d. thesis, Massachusetts Institute of Technology.

[21] Kottapalli, A. P., 2013, "Development of a body force model for centrifugal compressors," M.sc. thesis, Massachusetts Institute of Technology.

[22] Cao, T., Hield, P., and Tucker, P. G., 2017, "Hierarchical immersed boundary method with smeared geometry," *Journal of Propulsion and Power,* **33**(5), pp. 1151–1163.

[23] Kiwada, G. F., 2008, "Development of a body force description for compressor stability assessment," Ph.d. thesis, Massachusetts Institute of Technology.

[24] Benneke, B., 2009, "A methodology for centrifugal compressor stability prediction," M.sc. thesis, Massachusetts Institute of Technology.

[25] Eisenlohr, G., Krain, H., Richter, F.-A., and Tiede, V., 2002, "Investigations of the flow through a high-pressure ratio centrifugal impeller," In Proceedings of Turbo Expo: Power for Land, Sea, and Air, Vol. 5, pp. 649–657.

[26] Inc., A., 2019, *ANSYS Fluent Theory Guide, 2019R2* ANSYS Inc., Canonsburg, PA, USA.

[27] Reid, L., and Moore, R. D., 1978, Design and overall performance of four highly loaded, high-speed inlet stages for an advanced high-pressure-ratio core compressor Tech. Rep. NASA-TP-1337, NASA Technical Report, NASA Lewis Research Center, Cleveland, OH, United States, October.

[28] Toro, E. F., 2009, *Riemann Solvers and Numerical Methods for Fluid Dynamics: A Practical Introduction* Springer Berlin Heidelberg.

[29] Greitzer, E. M., Tan, C. S., and Graf, M. B., 2004, *Internal Flow: Concepts and Applications* Cambridge Engine Technology Series. Cambridge University Press, Cambridge.

[30] McKain, T. F., and Holbrook, G. J., 1997, Coordinates for a high performance 4:1 pressure ratio centrifugal compressor Tech. Rep. NASA-CR-204134, NASA Technical Report, Detroit Diesel Allison, Indianapolis, IN, United States, July.

[31] Urasek, D. C., Gorrell, W. T., and Cunnan, W. S., 1979, Performance of two-stage fan having low-aspect-ratio first-stage rotor blading Tech. Rep. NASA-TP-1493, NASA Technical Report, NASA Lewis Research Center, Cleveland, OH, United States, August.

[32] Aungier, R. H., 2000, *Centrifugal Compressors: A Strategy for Aerodynamic Design and Analysis* ASME Press, January.

APPENDIX: EQUATIONS FOR INFLUENCE COEFFICIENT ANALYSIS

The pressure gradient term is substituted by combining the differential form of the following equations:

Equation of state:

$$\frac{dP}{P} = \frac{d\rho}{\rho} + \frac{dT}{T} \tag{26}$$

Meridional area:

$$\frac{dA_m}{A_m} = \frac{dr}{r} \tag{27}$$

Continuity:

$$\frac{d\rho}{\rho} + \frac{A_m}{A_m} + \frac{dw}{w} + tan\beta d\beta = 0 \tag{28}$$

Gibb's equation:

$$\frac{\nabla s}{c_p} = \frac{\nabla T}{T} - \frac{\gamma - 1}{\gamma}\frac{\nabla P}{P} \tag{29}$$

Viscous force using Marble's expression:

$$F_{visc} = \frac{\partial s}{\partial l}T = \frac{\partial s}{\partial m}Tcos\beta \tag{30}$$

Relative stagnation temperature:

$$\frac{dT_{0,rel}}{T_{0,rel}} = \frac{dT}{T}\left[\frac{1}{1 + \dfrac{\gamma - 1}{2}\, Ma_{rel}^2}\right] + \frac{dw}{w}\left[\frac{(\gamma - 1)\, Ma_{rel}^2}{1 + \dfrac{\gamma - 1}{2}\, Ma_{rel}^2}\right]$$

Conservation of rothalpy:

$$dI = dh_{0,rel} - \frac{1}{2}d\left(\Omega^2 r^2\right) \tag{31}$$

By combining the above equations, the pressure gradient term $\partial P/\partial n$, is expressed in terms of other flow-field parameters:

$$\frac{1}{\rho}\frac{dP}{dn} = \frac{w^2}{(2\gamma - 1)\, Ma_{rel}^2 + 1}\left\{-F_{visc}tan\beta\frac{\dfrac{1}{Ma_{rel}^2} + (\gamma - 1)}{R\,(\gamma - 1)} + \frac{sin\phi sin\beta}{r}\left(\frac{Ma_{\Omega}^2}{Ma_{rel}^2} + 1\right) - sin\beta tan\beta\frac{\partial\beta}{\partial m}\right\} \tag{32}$$

Copyright © 2025 by Rolls-Royce plc;
reuse license CC-BY 4.0



https://dspace.org/

A new body force-based modelling approach for turbomachinery aerodynamics: formulation, verification and implementation aspects

Lamprakis, Dimitrios; Righi, Mauro; Pachidis, Vassilios

2025-06-16
American Society of Mechanical Engineers (ASME)
https://doi.org/10.1115/gt2025-153775
Lamprakis D, Righi M, Pachidis V. (2025) A new body force-based modelling approach for turbomachinery aerodynamics: formulation, verification and implementation aspects. In: Proceeding of the ASME Turbo Expo 2025: Turbomachinery Technical Conference and Exposition, 16-20 Jun 2025, Memphis, Tennessee, USA, Volume 11: Turbomachinery — Deposition, Erosion, Fouling, and Icing; Design Methods & CFD Modeling for Turbomachinery; Ducts, Noise & Component Interactions, Article number GT2025-153775

Downloaded from a DSpace repository. https://dspace.org/